

Validation analysis of the thermal and radiometric integrity of RIT's synthetic image generation model, DIRSIG

John E. Mason, John R. Schott

Rochester Institute of Technology, Center for Imaging Science
Digital Imaging and Remote Sensing Laboratory
Chester F. Carlson Building, 54 Lomb memorial Drive
Rochester, New York 14623-5604

Donna Rankin-Parobek

Eastman Kodak Company, 1447 St. Paul Street
Rochester, New York 14653

ABSTRACT

The Digital Imaging and Remote Sensing laboratory's Image Generation model, DIRSIG, was validated in the long wave infrared (LWIR, 8-13.3 μm) and midwave infrared (MWIR, 3-5 μm) pass bands. Truth data was collected for all components of the thermal and radiometric submodels including a complete set of meteorological and radiometric data. Truth temperatures were collected using a bank of thermistors and truth radiance images were collected with calibrated InSb (MWIR) and HgCdTe (LWIR) detectors. Sensor spectral response functions were also included in the radiometric analysis.

Relative error contributions to the total temperature/radiance digital count were investigated for each component in the multi-spectral model. Largest contributions were found to be wind speed, air temperature, visible emissivity, and fractional sky exposure for the thermal model and atmospheric transmission, temperature, and emissivity for the radiance model. An overall comparison of truth and synthetic images yields RMS errors of as low as 1.8° C actual temperature and 5°C (LWIR) and 6°C (MWIR) apparent temperature.

1. Background

Synthetic image generation (SIG) models are used to address a broad range of problems. They can be used as a tasking aid to determine what combination(s) of spectral range, look angle, time of day, etc., enhance the occurrence of a specific phenomenon (*i.e.* target recognition). Many different combinations can produce synthesized images in a cost-effective manner as compared to taking aerial training data. Other applications of SIG include sensor development, training, reverse engineering, and the evaluation of automated or semi-automated exploitation algorithms.

From a scientific standpoint, a major value of synthetic image generation is that it can provide a complete end-to-end model of the image chain. The extent to which a modeled scene matches an actual scene provides a measure of how well the imaging process is understood. Conversely, the mismatch between a modeled and an actual scene can provide clues to where our understanding of the physical or engineering principles is flawed. That is why it is essential to perform a validation analysis on a SIG model as a whole as well as on the sub-components which comprise the image chain. This manuscript details such an analysis on the Rochester Institute of Technology's (RIT) Digital Imaging and Remote Sensing (DIRS) laboratory's Synthetic Image Generation (DIRSIG) model.^{1,2,3}

This experiment represents the first test of the quantitative integrity of the DIRSIG model. As such, it is not intended to show how good or how bad the model is, but to point out limitations in the model and areas in need of attention as part of ongoing research and development activities to improve the SIG modeling process.

2. DIRSIG Model Overview

DIRSIG was originally written for the infrared region of the electromagnetic spectrum, but has since been expanded to include visible radiation. Its full range is 0.4-14 μm , and follows the image chain based primarily on first-order physical principles. A complete description of the model can be found in reference [2]. The validation of DIRSIG reported here only covers the LWIR (8-13.3 μm) and MWIR (3-5 μm) portions of the spectrum.

Fig. 1 gives a generalized block diagram of the submodels within DIRSIG. The geometry submodel contains the physical information of the objects in the target scene including spatial information (size, location, and orientation) and

material attributes (e.g. emissivity, conductivity, etc.). The ray-tracer submodel relates the target scene with the sensor and the source (e.g. look-angle, time-of-day, and spectral range). Rays are cast from sensor to target to determine the type of interaction involved (e.g. specular bounce to sky, specular bounce to background, diffuse hit, or ray cast to sky) and to gather the pertinent parameters for computing object temperature and impinging radiance. The sensor submodel takes the radiance information received at the front end of the sensor and passes it through a sensor response function.

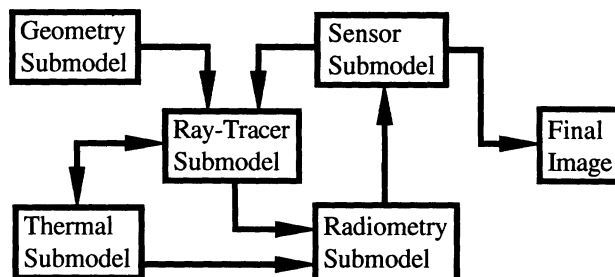


Fig. 1. Block diagram of the submodels within DIRSIG. Exchange of information is indicated by the solid lines with arrowheads showing direction of flow.

The other two submodels---the guts of DIRSIG---are the subject of this validation analysis. In the thermal submodel, surface temperatures of target objects are computed from temporal, meteorological, and material information. The thermal model incorporates a modified version of the Air Force Infrared Simulated Image Model (AIRSIM) known as THERM.^{4,5} In the radiometry submodel, atmospheric contributions to the radiance impinging on the target and sensor (e.g. transmission, upwelled and downwelled radiance, etc.) are extracted from a radiometric database created particularly for the time, location, and atmospheric condition of the synthetic scene. The radiometric database comprises spectral vectors of radiance components extracted from the output of the Air Force Geophysics Laboratory (AFDGL)/ Spectral Sciences Inc. MODTRAN Atmospheric Transmission/Radiance Code.^{6,7}

3. Validation Procedure

The validation of the thermal and radiometric submodels is divided into two parts. The first tests the sensitivity of DIRSIG to the numerous input parameters needed for THERM and the radiometry submodels. The second tests DIRSIG's overall absolute and relative accuracy in predicting object radiance values and temperatures. The method of determining the sensitivity of THERM differs from the method used for the radiometry submodel, since the radiance is computed through an analytical equation while the temperature is determined through numerical methods. Since object temperatures need to be determined before a total radiance value can be computed, the validation of THERM is presented first.

The identified input parameters for THERM, and the means by which a truth value could be measured or estimated for comparison, are listed in Table 1. The parameters can be put into two groups: weather (or environmental) parameters, which are external factors impacting an object's temperature, and object (or material) parameters, which are internal factors controlling an object's temperature. In order to reach a steady-state temperature for the time of day for which the image is formed, 24 hours of prior weather knowledge must be input to THERM. This weather data can also be predicted by THERM, given the proper location, time, date, and standard weather forecast data. Therefore, as part of the validation, THERM's weather predictions were also tested against meteorological data.

Truth temperatures and imagery was collected in two experiments including all of the parameters necessary for input to THERM and DIRSIG. The experiments ran for forty-eight hour periods on the dates of October 5, 6, and 7, 1990 and June 22 and 23, 1992. A diagram of the June 1992 experiment is shown in Fig. 2. Imagery was captured from the roof of the RIT Center for Imaging Science building in order to simulate airborne sensor collections. LWIR imagery was collected using an Inframetrics IR camera containing a single Mercury/Cadmium/Telluride (HgCdTe) detector which was cooled by liquid nitrogen to a temperature of 77K within a cryogenic dewar. The image was scanned using electromechanical servos. During each time interval, five frames of the image were grabbed using Werner Frei software on an Image Technology board. These frames were then averaged to reduce noise artifacts which appear in individual images.

MWIR imagery was also gathered during the June 1992 collection with a Platinum Silicide (PtSi) 2-D array video compatible IR imager⁸ supplied by the ARMY Night Vision Laboratory. Visible images were also collected using a CCD camera for purposes of determining facet sun/shadow histories during the October 1990 collection. Sun/shadow history is

used to better estimate object temperatures. During the June 1992 collection, four separate images in different bands (red, green, blue, and SWIR) were collected by the CCD camera using different filters. These images were used for a validation study of DIRSIG's predictions in the visible region of the electromagnetic spectrum.⁹ All images were collected every half hour, stored on computer hard drive, and backed up on magnetic tape.

Table 1 Thermal Sub Model Variables: Truth and Prediction Sources

Inputs to Thermal Model Environmental Prediction		Environmental Model Output Validation		Inputs to Thermal Model Temperature Prediction	
Value	Source	Value	Source	Value	Source
Sunrise Time	Longitude, Latitude, Day of Year from Ephemeris	Air Temperature	Thermometer	Density	Available Literature
Sunset Time		Air Pressure	Barometer	Specific Heat	Available Literature
Sunrise Air Temperature	Weather	Relative Humidity	Hygrometer	Thermal Conductivity	Available Literature
Peak Air Temperature	Service	Dew Point	*	Exposed Area	Estimate
Time of Peak Air Temperature	Report	Wind Speed	Anemometer	Visible Emissivity	Available Literature
Air Pressure		Direct Insolation	Pyronometer**	Thermal Emissivity	Emissometer
Humidity		Diffuse Insolation	Pyronometer**	Self-Generated Power	Available Literature
Dew Point		Sky Exposure	Estimate	Thickness	Measurement
Wind Speed		Cloud Type	Estimate	Slope	Measurement
Sky Exposure		Rain Type	Estimate	Azimuth	Measurement
Cloud Type		Rain Rate	Rain Gauge	Sun/Shadow History	Visible Imagery
Rain Type		Rain Temperature	Estimate	Plus all of the environmental model outputs and their corresponding experimental values as a function of time.	
Rain Rate	∨				
Rain Temperature	Engineering Estimate				

* Thermal model computes dew point based on air temperature and relative humidity

** Eppley Precision Pyronometers

† YSI Thermistors

Temperatures of objects in the scene were recorded by thermistors on fifteen minute intervals. The thermistors were calibrated using a water bath of known temperature. As a check, the thermal images taken with the LWIR sensor were converted via the Planck equation to apparent temperature. For both collections, object dimensions, angles and locations within the scene were measured, and radiosonde data was obtained from the Buffalo Airport for October 4-7, 1990 and June 22-24, 1992. To test THERM's weather parameter predictions, complete diurnal weather data from six days: June 23 and 24, 1987; October 6 and 7, 1987; and October 5 and 6, 1990, was used. Meteorological data was collected at fifteen minute intervals. The 1987 data were from an USAF collection at Wright Labs where similar ground truth data were available.¹⁰

3.1 Weather Parameters

Since the computation of temperature from environmental variables (and object parameters, for that matter) do not result from an analytic equation, a method was developed to determine THERM's sensitivity to variations in individual parameters. THERM was first run with the generic object and weather parameters to establish 'base' temperatures for all objects. The RMS error associated with one weather variable was randomly added to or subtracted from the time dependent nominal value in the weather file while all other variables remained nominal. An RMS error was computed between the new temperature output and the 'base' temperatures. Table 2 lists the predicted RMS (column A) and measured errors (column D) associated with the weather variables input to THERM and the RMS errors in output temperature resulting from these input errors (columns C and E, respectively). The truth data for the weather parameter tests were the temperatures of 11 objects as

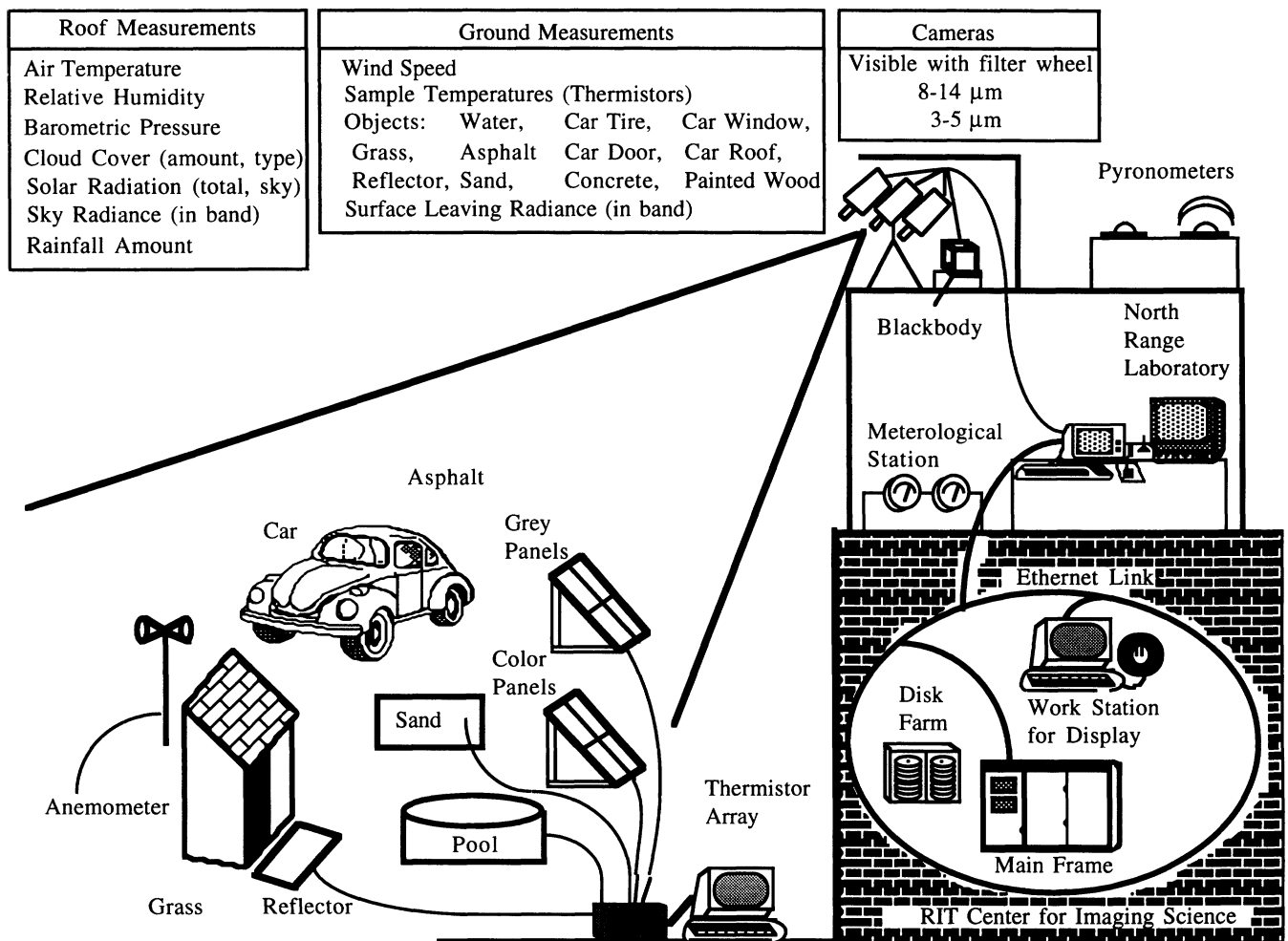


Fig. 2 Validation Experiment

computed by THERM using the measured diurnal weather files.

Note that for the prediction errors, both a bias value (column B of Table 2) and an RMS error are listed for each variable. For some variables, THERM tends to make optimistic or pessimistic predictions, resulting in a bias when compared to the actual data. For these cases, the bias was added to the true weather variable and then the RMS error was randomly added to or subtracted from the nominal weather parameter value.

The errors resulting from THERM's prediction of the weather are greater than those errors resulting from variability in the measured data. One way to improve upon the prediction errors is to edit THERM's output weather. If the user has some idea of the weather patterns for the day being modeled, he can adjust the data predicted by THERM. It must be noted that THERM predicts the weather well when modeling stable days such as a typical sunny day with few clouds. THERM cannot predict rapidly changing weather conditions because it only works from values averaged over a 24 hour period unless it is manually edited by the user (e.g. a forecast of a clear morning, and a cloudy afternoon, can be approximated to improve prediction performance). Depending upon the application of DIRSIG, this limitation may or may not be problematic. For training use and prediction of optimum imaging times, THERM's limitations are not critical. Many different scenarios can be defined with acceptable results from DIRSIG. However, in modeling of actual imagery collected under unknown or unmeasured conditions, the expected errors will increase.

The most important variables (i.e. those that have the greatest impact on the error in output temperature) are air temperature, wind speed, and direct and diffuse insolation. When running THERM in the predictive mode, the critical weather parameters should be paid particular attention. Also note that for either method of weather generation, wind speed should be carefully watched. Even relatively small changes in wind speed (which THERM cannot predict) or errors in

measured wind speed can have large effects on resulting object temperatures due to the convective cooling (or warming) nature of the wind.

Table 2 Weather Parameter Errors and Resulting Temperature Errors

	A	B	C	D	E
Variable	Prediction RMS Error	Prediction Bias	Temperature Error	Measurement Error	Temperature Error
Air Temperature (°C)	1.57	0.63	1.09	0.2	0.10
Air Pressure (mbar)	1.87	-0.05	0.002	0.2	0.002
Humidity (%)	0.14	0.05	0.18	0.2	0.007
Dew Point (°C)	3.57	1.46	0.27	NA	NA
Wind Speed (m/sec)	1.31	-0.02	0.31	1.11	0.30
Direct Insolation (%)	10.20	-4.47	0.91	Precision: 0.04 Accuracy: 0.2	0.006
Diffuse Insolation (%)	8.06	-3.16	1.68	Precision: 0.04 Accuracy: 2.0	0.005
Sky Exposure (as fraction)	0.21	0.00	0.36	0.05	0.07
Cloud Type (#)	1	0	0.14	0 if CT = 0,1,7,8 1 if CT ≠ 0,1,7,8	0.05
Precipitation Type (#)	None	NA	NA	None	NA
Precipitation Rate (cm/hr)	0.06	0.00	0.10	0.013	0.009
Precipitation Temperature (°C)	7.14	-5.35	0.16	2	0.014
Total Error (RSS) (no Rain) (°C)	-		2.27	-	0.33
Total Error (RSS) (rain) (°C)	-		2.28	-	0.33

3.2 Object Parameters

The objects chosen for validation were selected so that materials with various thermal properties were represented. Each of these materials had at least five different listings of objects parameters from which the predicted parameter variation was computed. When an object is being modeled and is not available for measurement, its intrinsic physical characteristics must be estimated. Lists of parameters for many different objects have been compiled for this situation.⁵ Many similar objects on these lists have varying parameters. The 'predicted' object parameter errors are the variations of each parameter within each group of materials. 'Measurement' errors of object variables are those associated with the accuracy and precision to which a variable can be measured in an experiment. Some object parameters such as thickness and orientation can be measured very precisely. Other values are in manufacturer specifications or general material property tables found in thermodynamic and heat transfer literature. However, these references rarely list the variance associated with the given parameter value. For those easily measurable parameters, the actual measurement accuracy and precision are listed in the error table. For the other variables, a conservative estimate of 10% error in the given value was used for the sensitivity testing. The tests were run in the same manner as the weather sensitivity tests: error was added to one parameter at a time, object temperatures were computed by THERM, then RMS errors between these output temperatures and the truth temperatures were calculated. The average error due to each variable over all objects is listed in Table 3.

The object parameters whose errors have the greatest impact on output temperatures computed by THERM are visible emissivity (*i.e.* solar absorption), exposed area, and azimuth angle. The error associated with self-generated power is misleading, since only passive facets were fully tested during this study. Therefore, this output temperature error is not a true representation of THERM's ability to predict temperatures of active facets. If active facets were included in this study, the temperature error would most likely be much higher. The high error due to prediction variability in thermal conductivity is due to one or two materials having a wide range of thermal conductivities listed in the literature. This large variability inflated the resulting temperature error. Comparing the error due to measurement variability of thermal conductivity to the error due to measurement variability in the other object parameters shows that the error due to thermal conductivity is not as critical as the errors in the variables listed above.

Error due to azimuth angle variability is easily understandable. The azimuth of a facet determines the amount of solar loading the facet receives throughout the day. Relatively small errors can significantly increase or decrease the amount of solar energy the facet receives, thus affecting the facet's temperature. Exposed area is a difficult parameter to deal with. It is

used as the fraction of the facet area exposed to the environment. This parameter is not measured in a straightforward manner, but is estimated by the user. Again, small changes in the exposed area can have a significant effect on the facet's temperature, since they significantly impact the radiation load on the surface.

Table 3 Object Parameter Errors and Resulting Temperature Errors

Variable	Prediction Error	Temperature Error	Measurement Error	Temperature Error
Specific Heat (L/cm/°C)	Varies	0.0188	10%	0.0718
Density (kg/m ³)	Varies	0.0865	10%	0.072
Thermal Conductivity (L-cm/hr/°C)	Varies	0.4362	10%	0.0477
Thickness (cm)	20%	0.1023	0.1	0.0363
Visible Emissivity (as fraction)	Varies	0.7774	10%	0.3934
Thermal Emissivity (as fraction)	Varies	0.1983	0.025 (~5%)	0.0624
Self-Generated Power (L)	Varies	0.2488	10%	0.0236
Exposed Area (as fraction)	20%	0.5634	10%	0.2809
Slope	7.5°	0.1219	3°	0.0456
Azimuth	7.5°	0.2905	3°	0.1012
Total Error (passive) (°C)	-	1.1265	-	0.5137
Total Error (active) (°C)	-	1.1536	-	0.5142

Note that the magnitudes of the errors due to measured errors in object parameters are greater than those of the errors due to measured weather parameter variability. This reinforces the statement that the object parameters should be the primary focus when running THERM with measured meteorological data. Assuming that the weather and object related temperature errors are independent, THERM's combined sensitivity to variations in weather and objects parameters for passive facets is: 2.54 °C (prediction) and 0.61°C (measurement).

When it is important to predict true object temperatures, the definition of accurate object parameters is critical. The values obtained in the literature are for generic or typical materials and do not account for things such as age or differing chemical composition which may effect the actual physical parameter. Therefore, a process of deriving optimum object parameters was created in order to correct documented material values for the specific targets observed in the experimental scenes.

In deriving optimum object parameters for the experimental scene, four parameters were varied to fine-tune THERM's output temperatures. These parameters were exposed area, visible emissivity, thickness and thermal conductivity. Visible emissivity is the fraction of visible insolation that is absorbed by a material. Exposed area is the fraction of an object's area which is exposed to environmental effects such as sun, sky, wind, and rain. The exposed area was adjusted based on the shadowing of a facet due to nearby objects. The thermal emissivity, slope, and azimuth were kept constant once the basic values were determined because they were known to sufficient accuracy. THERM combines the heat capacity (defined as the product of the material's specific heat and density) and thickness parameters into one variable, thermal mass, for its temperature calculations. Thermal mass is a measure of the resistance of a material to changes in its thermal environment. Another combined parameter is the Biot number, which is the product of thickness and the calculated heat transfer rate, divided by the object's thermal conductivity. It is a measure of the insulating properties of a material. When deriving optimal object parameters, the thickness was usually varied while the heat capacity was held constant to adjust an object's thermal mass. A byproduct of this procedure was a change in the Biot number. If this change produced undesirable effects, the thermal conductivity was varied to readjust the Biot number to a more reasonable value.

Once the other parameters were appropriately defined based on physical characteristics of the material, these four variables were adjusted individually and in combination for fine-tuning. The final combinations which resulted in the smallest RMS error (between computed and measured temperatures) were used as inputs to THERM. Table 4 lists the RMS errors computed between THERM's prediction of object temperatures (using either optimum parameters or generic parameters taken directly from available literature) and the actual object temperatures measured by thermistors. Temperatures were computed using both full meteorological data and forecast weather values predicted by THERM.

THERM predicts object temperatures quite accurately when the total weather history is known and the object parameters have been fine tuned to fit the actual objects in the scene. However, it is a rare situation in which all weather and object information is known. More realistically, the user will have generic object profiles and perhaps an outline of the weather

conditions for the day being modeled. In this case, THERM can generally predict object temperatures to within 3.5°C. It can be seen by comparison of the errors in Table 4 that it is very important to have a good profile of the object parameters.

Table 4 RMS Errors between Thermistor Truth and THERM Prediction Values for October 6, 1990 and June 23, 1992 (24 hours / day on 15 minute centers)

Object	Observed Meteorological Data		Predicted Meteorological Data	
	Optimized	Generic	Optimized	Generic
Aluminum*	1.23	1.52	1.67	5.06
Asphalt**	2.31	4.33	5.05	8.14
Brick*	1.78	1.90	2.06	5.00
Car Roof (white)*	1.63	2.09	2.93	5.94
Car Side (white)*	2.91	4.59	2.52	4.15
Car Window**	2.49	8.44	7.78	10.58
Concrete Panel*	1.04	1.13	1.70	5.25
Roof Gravel*	1.36	1.59	1.35	5.30
Sand**	1.14	1.45	4.90	5.21
Tire**	3.36	6.22	9.49	7.28
Water*	1.05	3.45	1.62	7.24
Windshield**	2.27	7.24	5.03	9.39
Wood Panel*	1.23	1.77	1.54	7.13
Average Error	1.83	3.52	3.66	6.59

* 10/6/90 only (cloudy, low dynamic range)

** Parameters optimized for 6/23/92 (partly cloudy, high dynamic range), results include RMS errors for targets on both days

4. Radiometry Validation

Since DIRSIG is a versatile SIG program, able to simulate a scene from a variety of known and unknown information, four error types were defined for the sensitivity analysis. Ideal errors (I) include factory specifications of the instrumentation used to collect truth data with the assumption that the model is error free. THERM measurement errors (M) were determined using measured environmental data and optimal object parameters to predict best-case object temperatures. THERM prediction errors (P) were determined using predicted weather data and generic object parameters to determine worst-case object temperatures. The final error set, clouds/daytime (C/D), includes errors induced in the radiometric variables by LOWTRAN7 when clouds were present in the actual scene (LWIR), or when the image is synthesized during daylight hours (MWIR). These last three error types use DIRSIG and truth data comparisons to determine the error of the individual quantity.

The general equation for governing radiance is given by:

$$L = \left\{ \varepsilon L_T + (1 - \varepsilon) \left[I_T \frac{E_S}{\pi} \tau_1 \cos(\theta_S) + FL_D + (1 - F) \left(\varepsilon_B L_{TB} + I_B \frac{E_S}{\pi} \tau_1 \cos(\theta_S) (1 - \varepsilon_B) \right) \right] \right\} \tau_2 + L_u \quad (1)$$

where the sources for input into the radiometry submodel, and measured or estimated sources for comparison, are defined below in Table 5 and described in the following subsections.

All variables were taken to be independent with the exception of τ_2 and L_u , which are inversely correlated. Standard error propagation techniques were used for sensitivity analysis using the independent and correlated variables.¹¹ The error in total radiance is

$$\sigma_L = \sqrt{\sum_x \left(\frac{\partial L}{\partial x} \sigma_x \right)^2 + 2(xterm)}; x = \varepsilon, L_T, I_B, I_T, E_S, \pi \times \tau_1, \theta_S, F, L_D, L_u, L_{TB}, \theta_B, \varepsilon_B, \tau_2. \quad (2)$$

where $\frac{\partial L}{\partial x}$ is the partial derivative of L with respect to variable x , σ_x is the error in variable x , and

$$xterm = \rho_{L_U \tau_2} \left(\frac{\partial L}{\partial L_U} \right) \left(\frac{\partial L}{\partial \tau_2} \right) \sigma_{L_U} \sigma_{\tau_2} \quad (3)$$

is the cross-term in terms of the correlation coefficient,

$$\rho_{L_U \tau_2} = \frac{1}{k \sigma_{L_U} \sigma_{\tau_2}} \sum_{n=1}^k (\Delta L_U)_n (\Delta \tau_2)_n \quad (4)$$

with $(\Delta x)_n$ the difference of truth and test values for variable x in time period n of k total time periods. The resulting cross term is negative so it reduces the overall error in radiance by correcting for the independent error contributions of the inversely correlated variables. The correlation coefficient between τ_2 and L_U was determined to be -0.96 in the LWIR region and -0.98 in the MWIR region.

Table 5 Radiometry Submodel Variables: Truth and Prediction Sources

Inputs to Radiometry Submodel		Validation
Value	Source	Source
ϵ - Target Emissivity	DIRS Database	Emissometer
L_T - Target Radiance due to Temperature	Thermal Submodel	Thermistor
I_T & I_B - Sun/Shadow Histories	Ray tracer Submodel	Visible Imagery
$E_s/\pi \tau_1$ - Solar Insolation	LOWTRAN	Pyronometer*
θ_s - Target Slope	Geometry Submodel	Measurement
F - Shape Factor	Geometry Submodel	Estimate
L_D - Downwelled Radiance	LOWTRAN	Spectroradiometer**
L_{TAB} - Ave. Background Radiance due to Temperature	Thermal Submodel	Thermistor
θ_B - Background Slope	Geometry Submodel	Measurement
ϵ_B - Background Emissivity	DIRS Database	Emissometer
τ_2 - Target-Sensor Transmission	LOWTRAN	Radiometric Ground Truth
L_U - Directional Upwelled Radiance	LOWTRAN	Radiometric Ground Truth
L_D^{\wedge} - Directional Downwelled Radiance	LOWTRAN	Spectroradiometer**
L_{TB} - Background Radiance due to Temperature	Thermal Submodel	Thermistor

* Eppley Precision Pyronometer

** Infrared Systems Spectroradiometer

Four ray-interaction types are modeled within DIRSIG, as cast from the sensor to a target object. Examples of objects used in the analysis for each case are given in parentheses. In Case 1, the ray hits a diffuse target (grass). When this occurs, L_{TAB} replaces L_{TB} in Eq. 1 as the average thermal radiance of all the background objects which are in the direct line-of-sight of the target hit point and L_D is the integrated sky radiance. In Case 2, the ray hits a specular target (water), and reflects to the sky. Here, L_D is the directional downwelled sky radiance (\hat{L}_D) and $F = 1$, so the background terms in Eq. 1 are eliminated. In Case 3, the ray hits a specular object (asphalt) and reflects to hit a background object (car door) and $F = 0$. In Case 4, the ray completely misses the scene---so the only contribution to the total radiance is the directional upwelled radiance term, L_U . In making individual radiometric parameter sensitivity analyses, the wavelength-dependent quantities had to be integrated over the appropriate band pass. Therefore, the errors represent the average error.

4.1 Emissivity (ϵ_S , ϵ_B):

The normal and angular emissivities of many objects in the ray-traced scene were measured using emissometers developed at RIT.¹² The error in these measured angular emissivities is 0.025 emissivity units (Ideal, Measured). For targets for which no emissivity data were available, angular emissivity was approximated by using values from similar objects which have been measured. The resulting prediction error (P, C/D) is estimated to be 0.05 emissivity units.

4.2 Thermal Radiance (L_T , L_B , L_{TAB}):

The error in thermal radiance was determined three ways: actual measurements of object temperatures with thermistors (I), predicted temperatures via THERM using optimal parameters (M), and using generic parameters (P, C/D). Propagation of these temperature errors through Planck's equation yields the errors in radiance due to temperature. These errors are listed in Table 6

Table 6 Radiance Error Resulting from Error in Object Temperature for an Object at 300K

Error Type	T (°C)	LWIR		MWIR	
		L (W/m ² -sr)	% Error	L (W/m ² -sr)	% Error
Thermistor (I)	300 ± 0.14	54.84 ± 0.10	0.2%	1.506 ± 0.007	0.5%
THERM (M)	300 ± 0.61	54.8 ± 0.5	0.9%	1.51 ± 0.03	2.0%
THERM (P)	300 ± 2.54	54.8 ± 1.9	3.6%	1.51 ± 0.14	9.0%

4.3 Shape Factor (F):

The shape factor is the percentage of sky exposure as viewed from the target. It is determined through the ray tracing submodel and its value is the ratio of the number of hits to sky to the number of rays cast over the hemisphere. A conservative estimate of the error in the ray tracer submodel for sky exposure, as compared to the actual sky exposure, is 10% for the ideal case (I), 20% for the other cases (M, P, C/D).

4.4 Solar Insolation ($E_S * \tau_1 * \cos(\theta) / \pi$):

LOWTRAN7's prediction of solar insolation was compared to pyronometer data taken during the data collections. The pyronometer was sensitive in the 0.285-2.8 μm region. An RMS error over time between the pyronometer data and these predicted values was then computed. It is assumed that the prediction error in other passbands (MWIR) is proportional to this error, so a percent error was determined by dividing the RMS error by the range in insolation values.

LOWTRAN7 predicts well on cloud-free days, with an average error of 17.7% (M, P). However, errors as high as 50% occur for "cloudless day" predictions of cloudy days (C/D). For the ideal case (I), instrument specifications were used. In the LWIR region of the electromagnetic spectrum, the exoatmospheric solar radiance (E_S) is negligible.

4.5 Downwelled Radiance (L_D^* , L_D):

Directional downwelled radiance measurements were made as a function of wavelength with an Infrared Systems Spectroradiometer. Measurements were made at zenith angles of 8, 30, 45, 60, and 90 degrees, at each azimuth angle of 0, 90, 180, and 270 degrees (North, East, South, and West, respectively). Since the scattered solar radiance is negligible in the LWIR bandpass, the directional downwelled radiance is azimuthally invariant ($L_D(\text{West}) = L_D(\text{East})$, etc.). On relatively cloud-free days, the comparison of truth and predicted L_D is relatively good. However, on a day were clouds roll in from the west with the sensor facing west, LOWTRAN7's computation of L_D becomes progressively worse compared to truth, since no cloud data was input to LOWTRAN7.

Prediction error of downwelled radiance is assumed to be proportional to the errors in directional downwelled radiance over all zenith and azimuth angles. In the LWIR band pass, the percent error for L_D is 18.8% for cloud-free days (M, P). For cloudy days, this error is as high as 60% (C/D).

In the MWIR measurements, a noticeable difference occurs between daytime collection and nighttime collection. At night, the directional downwelled radiance looks similar to the LWIR case, with the radiance being approximately azimuthally invariant. During the day, however, since solar information is important in the MWIR region, the directional downwelled radiance is no longer azimuthally invariant, but depends upon the location of the sun. In the MWIR band pass, the error in L_D is 12.7% at night (M, P) and 54% in the daytime (C/D). For both MWIR and LWIR, ideal errors (I) were taken from instrument specifications. This error was determined to be 2% from the available spectroradiometer documentation.

4.6 Upwelled Radiance and Atmospheric Transmission (L_U , τ_2):

The radiance leaving the surface objects in the scene was measured on the ground using hand-held field radiometers (L_{ground}). At the same time, the scene was imaged by the Inframetrics (LWIR) and Mitsubishi (MWIR) cameras. Digital counts of the targets measured on the ground were extracted from the images. The radiance reaching the sensor was

computed from the digital counts using blackbody calibration data (L_{Sensor}). L_U and τ_2 were then determined through

$$L_{\text{sensor}} = L_{\text{ground}} \tau_2 + L_u \quad (6)$$

where τ_2 is the atmospheric transmission along the path from target to sensor and L_U is the upwelled radiance. The ground and sensor radiance values for all targets were plotted for certain objects in the scene so that the slope of the resulting line is τ_2 and the y-intercept is L_U . The error between LOWTRAN's prediction of τ_2 and the measured τ_2 values is 3.2% (LWIR) and 8.5% (MWIR) for all error types. Note that the path lengths here are very short and these errors may not be indicative of errors over longer path lengths.

Variations in the surface leaving radiance due to wind, changing cloud cover, and the angle at which the radiometer was held during measurements resulted in a large error in the measurement of L_{sensor} . Errors which caused slight variations in the slope (τ_2) resulted in large errors in the extraction of the intercept (L_U) since the data used was relatively far from the intercept. Therefore, the computed L_U values were unacceptable. Due to the similarity of the physics involved in modeling upwelled and downwelled radiance, it is reasonable to assume that the errors in LOWTRAN's prediction of directional upwelled radiance are proportional to the prediction errors of directional downwelled radiance, so these errors were used.

4.7 Target-to-Sensor and Target-to-Background Angles (θ_S, θ_B):

As in the thermal submodel testing, measurement errors of the target-sun path angles for both primary and background targets were estimated at $\pm 3^\circ$ (I), while unmeasured or simulated targets were estimated to be $\pm 7.5^\circ$ (M, P, C/D).

4.8 Sun/Shadow Ratio (I_T, I_B):

Investigation of the shadows in the visible images taken during the data collections and the ray-traced shadows in DIRSIG output images indicate that the ray-tracer correctly predicts the placement of sun shadows over time. Therefore, the error in the sun/shadow history flag was set to zero.

Table 7 is a summary of the measured or estimated errors of the terms in Eq. 1, while Tables 8 and 9 show the contribution to the total radiance error from each parameter as propagated through Eq. 1 through Eqs. 2-4 for each ray interaction type. Case 4 (ray missing scene) is not included in Tables 8 and 9 because for this case, $\sigma_L = \sigma_{L_U}$ and, in the validation process, no rays missed the scene (*i.e.* no sky was seen in the sensor's FOV). Equivalent apparent temperature is listed in parentheses in Tables 8 and 9.

Table 7 Individual Radiometric Variable Errors

	Error Type	ϵ_s, ϵ_B	L_T, L_B, L_{TAB}	F	$E_s \tau_1 \cos(\theta)$	L_D, L_D^*, L_U	τ_2	θ_S, θ_B
L W I R	Ideal	0.025	0.2%	10%	---	2%	3.2%	3.0°
	Measured	0.05	1.5%	20%	---	18.8%	3.2%	7.5°
	Predicted	0.05	3.6%	20%	---	18.8%	3.2%	7.5°
	Cloud	0.05	3.6%	20%	---	60%	3.2%	7.5°
M W I R	Ideal	0.025	0.5%	10%	0.2%	2%	8.5%	3.0°
	Measured	0.05	3%	20%	17.7%	12.7%*	8.5%	7.5°
	Predicted	0.05	9%	20%	17.7%	12.7%*	8.5%	7.5°
	Clouds/ Daytime	0.05	9%	20%	50%†	54%**	8.5%	7.5°

* Night time

** Day time

† Clouds

In the LWIR region, the main contributors to the error in radiance are τ_2 (especially for cases I and M), ϵ , and L_T (especially for cases P and C). For cloudy days, the error in L_U becomes important, which reflects the need for a better modeling of clouds in the LWIR window to produce more accurate sky radiance values. In the MWIR region, the main errors in radiance come from τ_2 , xterm, L_U (M), and L_T (P, C/D). The error contribution from xterm is large, due, in part, because the error in L_U is large. Consequently, the value of the xterm helps offset the errors in L_U and τ_2 . The effects of the xterm are felt more strongly in the MWIR bandpass and are probably the strongest contributor to the MWIR apparent temperature errors being lower than those for the LWIR bandpass in some cases.

Table 8 Error Contributions in $W/m^2\text{-sr}$ for LWIR Radiometry Variables. Overall rankings are listed for each variable. The total radiance is converted to temperature ($^{\circ}C$) through Planck's equation and is listed in parentheses.

Variable	Case 1 (Diffuse hit)				Case 2 (Specular hit)				Case 3 (Specular bounce)				Rank
	I	M	P	C	I	M	P	C	I	M	P	C	
ϵ	0.70	0.70	1.40	1.40	0.57	0.57	1.15	1.15	0.31	0.31	0.62	0.62	2
L_T	0.08	0.53	1.47	1.47	0.06	0.43	1.18	1.18	0.08	0.56	1.54	1.54	3
F	0.38	0.75	0.75	0.75	---	---	---	---	---	---	---	---	4
L_D, L_D^A	0.03	0.28	0.28	0.63	0.07	0.65	0.65	1.47	---	---	---	---	6
τ_2	1.0	1.0	1.0	1.0	0.75	0.75	0.75	0.75	1.22	1.22	1.22	1.22	1
L_U	0.02	0.16	0.16	0.54	0.02	0.16	0.16	0.54	0.02	0.16	0.16	0.16	8
ϵ_B	---	---	---	---	---	---	---	---	0.11	0.11	0.23	0.23	7
L_{TB}	---	---	---	---	---	---	---	---	0.01	0.05	0.13	0.13	9
- (xterm)	0.002	0.215	0.062	0.234	0.003	0.122	0.225	0.174	0.008	0.089	0.089	0.150	5
L	1.28 (1.92)	1.53 (2.29)	2.38 (3.57)	2.43 (3.65)	0.95 (1.43)	1.13 (1.74)	1.90 (2.85)	2.32 (3.48)	1.26 (1.89)	1.33 (2.00)	2.04 (3.06)	2.01 (3.02)	

Table 9 Error Contributions in $W/m^2\text{-sr}$ for MWIR Radiometry Variables. Overall rankings are listed for each variable. The total radiance is converted to temperature ($^{\circ}C$) through Planck's equation and is listed in parentheses.

Variable	Case 1 (Diffuse hit)				Case 2 (Specular hit)				Case 3 (Specular bounce)				Rank
	I	M	P	C/D	I	M	P	C/D	I	M	P	C/D	
L_U	0.011	0.067	0.067	0.325	0.010	0.063	0.063	0.297	0.010	0.062	0.062	0.294	3
L_D, L_D^A	0.000	0.003	0.003	0.013	0.007	0.046	0.046	0.218	---	---	---	---	6
$E_s \tau_1 / \pi$	0.000	0.004	0.004	---	0.000	0.038	0.038	---	0.000	0.017	0.017	---	8
L_T	0.008	0.048	0.144	0.135	0.005	0.032	0.095	0.091	0.025	0.147	0.442	0.442	4
L_{TB}	0.000	0.001	0.002	0.001	---	---	---	---	0.001	0.003	0.001	0.010	10
θ_s	0.001	0.004	0.004	---	0.015	0.036	0.036	---	0.004	0.010	0.010	0.010	7
θ_b	---	---	---	---	---	---	---	---	0.000	0.001	0.001	0.001	12
F	0.001	0.002	0.002	0.001	---	---	---	---	---	---	---	---	9
ϵ	0.013	0.013	0.027	0.003	0.017	0.017	0.035	0.007	0.057	0.057	0.115	0.173	5
ϵ_B	0.000	0.000	0.001	---	---	---	---	---	0.001	0.001	0.003	0.006	11
τ_2	0.141	0.141	0.141	0.131	0.138	0.138	0.138	0.120	0.438	0.438	0.438	0.408	1
-xterm	0.001	0.009	0.009	0.042	0.001	0.009	0.009	0.035	0.004	0.026	0.026	0.117	2
L	0.132 (1.71)	0.092 (1.19)	0.165 (2.14)	0.241 (3.17)	0.126 (1.67)	0.090 (1.19)	0.126 (1.68)	0.287 (4.07)	0.433 (2.59)	0.410 (2.46)	0.594 (3.55)	0.477 (2.97)	

To reduce the error in τ_2 , LOWTRAN7's prediction of atmospheric variables must be optimized. The intervening atmosphere can be well defined by using radiosonde data either from the location and day being predicted or data characteristics of the day being modeled. The inversion layer near the earth's surface can be corrected by using air temperature, air pressure, and dew point values measured on the ground. Predictions made for clear, cloud-free days also reduce the error not only in τ_2 , but also in the upwelled and downwelled radiance terms, when compared to predictions for cloudy days.

The emissivity error can be reduced by expanding the database of existing measured emissivities. Reduction of this error results in approximately a 50% reduction in the emissivity error contribution to final radiance error (*cf.* Table 7). As a result, the error in final radiance would be reduced by 20% when measured emissivity values are used.

The error of F was exaggerated in the sensitivity analysis (*cf.* Table 7). This error has since been reduced by developing a search routine which casts out rays from the target at different angles and directions. This routine determines any neighboring occluding objects and computes an estimate of the percentage of sky the facet 'sees', thus eliminating the

guesswork on the part of the user. This routine was implemented for the MWIR analysis.

Another important consideration for final radiance error reduction is accurate temperature prediction (LWIR) and atmospheric modeling (MWIR). Primarily, object parameters must be well defined. When at all possible, measured data should be used. Suggestions for improvement include a more advanced thermal model which would include temperature effects from adjacent objects, while still maintaining a sound basis of first principle physics for ease of object parameter description. Increasing the available database of not only emissivity values, but of all object parameters would also aid in error reduction by eliminating the guesswork in assigning facet parameters.

5. Absolute and Relative Radiometric Validation

For the overall comparison between DIRSIG and truth radiance values, DIRSIG was run using measured weather data and optimal material parameters to generate images over a 24-hour period. Figures 3 and 4 show actual truth and DIRSIG images at 10am, EDT, for LWIR and MWIR passbands, respectively. Visually, comparison between truth and DIRSIG is very good. An RMS error over time of the difference between DIRSIG and truth radiance values was determined for each object in the scene. In order to compare both MWIR and LWIR RMS radiance values on a similar scale, radiance values were converted to % radiance error by dividing RMS error by the average (truth) radiance over the time range for each object (cf. Fig. 5). On average, the % RMS MWIR radiance error is 10% higher than that for the LWIR bandpass. The radiance RMS error was also converted to an apparent temperature error through Planck's equation to gain a better physical intuition of DIRSIG's comparison with truth (cf. Fig. 6). The average RMS apparent temperature error is 5°C (LWIR) and 6°C (MWIR) and includes errors from the thermal model.

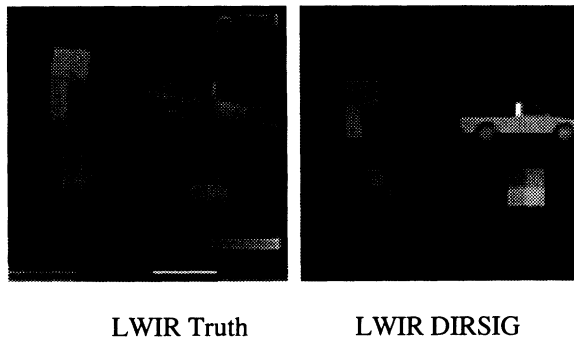


Fig. 3 LWIR Validation images for 10am EDT.

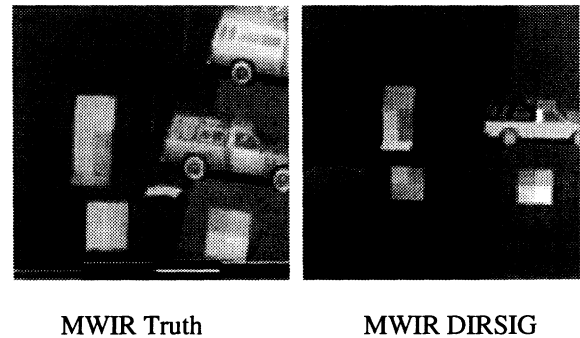


Fig. 4 MWIR truth DIRSIG images for 10am EDT.

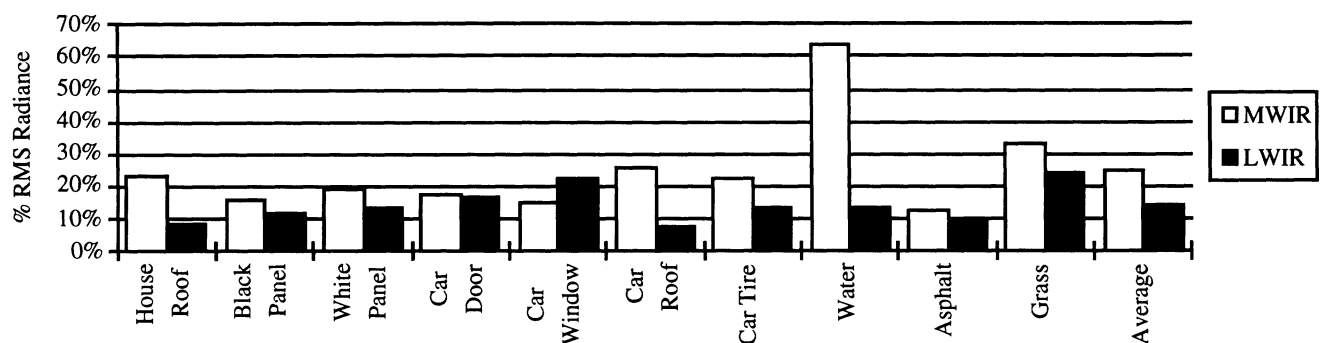


Fig. 5 RMS radiance error as a percent of average truth radiance

In theory, the errors displayed in Figs. 5 and 6 should be comparable to those predicted for the THERM measurement mode (M). However, June 23 was a partly cloudy day with cloud amounts increasing during the afternoon. Therefore, the results in Figs. 5 and 6 are more comparable to a combination of the M and C/D propagation methods. It must be noted that the theoretical error propagation serves more as a sensitivity indicator than as a predictor of absolute radiance error.

One thing that stands out in Figs. 5 and 6 is that while the RMS apparent temperature error in the radiance measured from the water target is lowest in the LWIR bandpass, it is the highest in the MWIR bandpass. A plot of truth vs. DIRSIG

radiance for water in the MWIR bandpass shows that the major contributor of the error in DIRSIG radiance occurs during sunlit hours. In addition, since the RMS temperature error and the RMS apparent temperature error in the LWIR bandpass is low, the errors in the water radiance are most likely due to the spectral components of the radiometry. Most notably, the emissivity for water for the view angle in the scene in the LWIR is 0.97 emissivity units, compared to 0.71-0.73 emissivity units in the MWIR. This implies that the emissivity of the water in the MWIR may be too low (making the reflectance too high). The effects of a too-high reflectivity are to under emphasize the temperature of the object in the total radiance equation and over emphasize the contributions of sky radiance, thus driving up the value of total radiance. Similar effects are seen in the plots of the red panel and of sand objects. These effects are reduced at night.

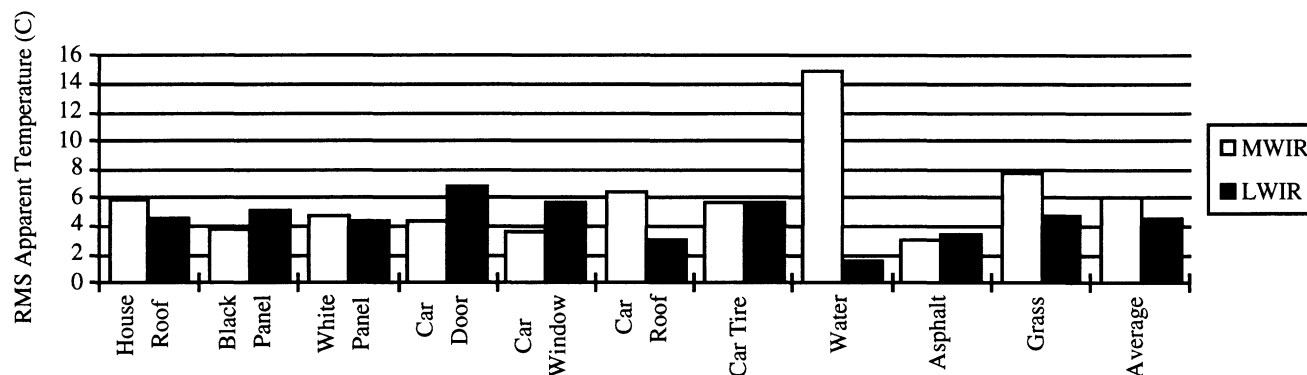


Fig. 6 RMS apparent temperature error

In summary, the overall validation of DIRSIG gives positive results. Not only can the model produce realistic looking scenes, it also produces radiometrically correct images to within 5°C (LWIR) and 6°C (MWIR) apparent temperature. As it exists now, DIRSIG is a very powerful tool in modeling synthetic images. Using this validation of a truth test image, we can now expand scene composition and scenarios with confidence, changing weather, time of day, season, climate, look angle, and a variety of other parameters to mimic different imaging conditions.

Most importantly, this validation has also shown us what areas of DIRSIG are weak and could use more work. Steps are underway already to put clouds directly into DIRSIG scenes for more accurate thermal and radiance computations as compared to LOWTRAN7's and THERM's blanket treatment of clouds. A more in-depth study of reflectance of objects, including full BDRF scans of materials, should lead to better reflectivity (and emissivity) assessment as well as a determination of diffuse and specular components. More accurate angular IR emissivity measurements for materials in the MWIR bandpass are needed--especially for sand and water. Other improvements to the existing model should include laterally conducting thermal computations, where each facet's temperature is altered by its neighbor's, adding a time-dependency to self-generated power (active facets) so that residual heat from an inactive source which was active in the past can be imaged, and adding motion to objects in a scene.

Finally, we should point out that this paper has emphasized absolute temperature and radiance errors. In many cases, it is much more important for the relative contrast between objects, or the rank order¹³ among several objects, to be correct. An assessment of DIRSIG relative to this rank order criteria has also yielded very positive results.¹⁴

6. Acknowledgments

This work was supported by the Office of Development and Engineering of the Central Intelligence Agency. Their support has allowed us to implement our ideas from an "infant" stage to a code which allows us to visualize the physics we think about everyday.

7. References

1. Schott, J. R., R. Raqueno, C. Salvaggio, "Incorporation of a Time-Dependent Thermodynamic Model and a Radiation Propagation Model into Infrared Three-Dimensional Synthetic Image Generation", *Optical Engineering*, Vol. 37, No. 7, 1505, July 1992.
2. Schott, J. R., J. E. Mason, C. Salvaggio, J. D. Sirianni, R. A. Rose, E. O. Kulp, D. K. Rankin, "DIRSIG - Digital imaging and remote sensing image generation model: description, enhancements, and validation," RIT/DIRS Report 92/93-51-146, July, 1993.

3. Rankin, D. K., "Validation of DIRSIG, an Infrared Synthetic Scene Generation Model," M.S. Thesis, Rochester Institute of Technology, February, 1992.
4. DCS Corporation, "AIRSIM thermal signature and prediction analysis tool definition and analysis of object inputs," DCS Technical Note 9090-002-004, DCS Corporation, December, 1990.
5. DCS Corporation, "AIRSIM thermal signature prediction and analysis tool model assumptions and analytical foundations," DCS Technical Note 9090-002-001 DCS Corporation, December, 1991.
6. Berk, A., L.S. Bernstein and D. C. Robertson, "MODTRAN: A moderate resolution model for LOWTRAN 7," GL-TR-89-0122, Spectral Sciences Inc., April, 1989.
7. Kneizys, F. X., E. P. Shettle, L. W. Abreu, J. H. Chetwynd, G. P. Anderson, W. O. Gallery, J. E. A. Selby and S. A. Clough, "Users Guide to LOWTRAN7," AFGL-TR-88-0177, Environmental Research Papers, No. 1010, Air Force Geophysics Laboratory, Optical/Infrared Technology Division, Hanscom AFB, MD, December, 1988.
8. Fujino, S. T., Miyoshi, M. Yokoh and T. Kitahara, "Mitsubishi thermal imager using the 512x512 PtSi focal plane array," *Proceedings of the SPIE, Infrared Technology*, Vol. 1157, San Diego, CA, 1989.
9. Stark, R. B., "Synthetic Image Generator Model: Application of Specular and Diffuse Reflectivity Components and Performance Evaluation in the Visible Region", M.S. Thesis, Rochester Institute of Technology, September, 1993.
10. Spector, D.N., P.F. Lambeck, S.L. Sheller, S.C. Sawtell, D.K. Rankin and J.R. Schott, "Air Force infrared simulated image models," *Proceedings of the Infrared Information Symposia*, Vol. 35, 1991.
11. Beers, Y., *Introduction to the Theory of Errors*, Addison-Wesley Publishing Company, Inc., Reading, MA, 1957.
12. Schott, J.R., M. Fairchild, X. Feng, R. Raqueno, B. Brower and T. Gallagher, "Techniques for measurement of the optical properties of materials," RIT/DIRS 89/90-51-134, Rochester Institute of Technology, January, 1990.
13. Lehmann, E. L., and H. J. M. D'Abrera, *Nonparametrics-Statistical Methods Based on Ranks*, Holden-Day, Inc., San Francisco, CA, 1975
14. Mason, J. E., J. R. Schott, C. Salvaggio, "Analysis of RIT's Digital Imaging and Remote Sensing Laboratories Synthetic Image Generation Model With Respect to Real-World Phenomena", to be submitted to *Proceedings of the SPIE, Infrared Technology*, San Diego, CA, July 1994.